ApJ, in press
Preprint typeset using LaTeX style emulateapj v. 5/2/11

DEEP X-RAY OBSERVATIONS OF THE YOUNG HIGH-MAGNETIC-FIELD RADIO PULSAR J1119−6127 AND SUPERNOVA REMNANT G292.2−0.5

C.-Y. Ng[1], V. M. Kaspi[1], W. C. G. Ho[2], P. Weltevrede[3], S. Bogdanov[4], R. Shannon[5], and M. E. Gonzalez[6]

ApJ, in press

ABSTRACT

High-magnetic-field radio pulsars are important transition objects for understanding the connection between magnetars and conventional radio pulsars. We present a detailed study of the young radio pulsar J1119−6127, which has a characteristic age of 1900 yr and a spin-down-inferred magnetic field of 4.1×10^{13} G, and its associated supernova remnant G292.2−0.5, using deep *XMM-Newton* and *Chandra X-ray Observatory* exposures of over 120 ks from each telescope. The pulsar emission shows strong modulation below 2.5 keV, with a single-peaked profile and a large pulsed fraction of 0.48 ± 0.12. Employing a magnetic, partially ionized hydrogen atmosphere model, we find that the observed pulse profile can be produced by a single hot spot of temperature 0.13 keV covering about one third of the stellar surface, and we place an upper limit of 0.08 keV for an antipodal hot spot with the same area. The nonuniform surface temperature distribution could be the result of anisotropic heat conduction under a strong magnetic field, and a single-peaked profile seems common among high-B radio pulsars. For the associated remnant G292.2−0.5, its large diameter could be attributed to fast expansion in a low-density wind cavity, likely formed by a Wolf-Rayet progenitor, similar to two other high-B radio pulsars.

Subject headings: ISM: individual objects (G292.2−0.5) — ISM: supernova remnants — pulsars: individual (PSR J1119−6127) — stars: neutron — X-rays: ISM

1. INTRODUCTION

Over the past two decades, our understanding of neutron stars has been revolutionized due to discoveries of several new classes of objects (see Kaspi 2010, for a review). An extreme class is magnetars, which typically have high spin-down-inferred magnetic fields[7] of 10^{14}–10^{15} G and show violent bursting activities (see Rea & Esposito 2011; Mereghetti 2008; Ng et al. 2011; Scholz et al. 2012). It is generally believed that their X-ray emission is powered by the decay of ultra-strong magnetic fields (Duncan & Thompson 1992; Thompson & Duncan 1995, 1996). However, the origin of magnetars and their relation to the more conventional rotation-powered pulsars remains a puzzle. The distinction between these two classes of objects became increasingly blurred thanks to the recent discoveries of a relatively low B-field magnetar of $B < 7.5 \times 10^{12}$ G (Rea et al. 2010), magnetar-like bursts from a rotation-powered pulsar (Gavriil et al. 2008; Ng et al. 2008a; Kumar & Safi-Harb 2008), and radio emission from magnetars (Camilo et al. 2006, 2007; Levin et al. 2010). These provide some hints that magnetars and radio pulsars could be drawn from the same population, and the former could represent the high-field tail of a single birth B-field distribution (Kaspi & McLaughlin 2005; Perna & Pons 2011; Ho 2012). One way to test this "unification" picture is via observations of high-magnetic-field radio pulsars,[8] which are a critical group of rotation-powered pulsars that have similar spin properties as magnetars, implying magnetar-like dipole B-field strengths (see Ng & Kaspi 2011, for a review). These pulsars could represent transition objects that share similar observational properties with magnetars and radio pulsars, providing the key to understanding the connection between the two classes.

PSR J1119−6127 is a young high-B radio pulsar discovered in the Parkes Multibeam Pulsar Survey (Camilo et al. 2000). It has a spin period $P = 408$ ms and a large period derivative $\dot{P} = 4.0 \times 10^{-12}$, which together imply a surface dipole B-field of 4.1×10^{13} G. It is one of the very few pulsars with a measured braking index.[9] Weltevrede et al. (2011) reported $n = 2.684 \pm 0.002$ using over 12 years of radio timing data, which give a characteristic age of $P/[(n-1)\dot{P}] = 1.9$ kyr. The true age could even be younger if the pulsar were born with a spin period close to the present-day value and n is constant. The pulsar is associated with a $17'$-diameter radio supernova remnant (SNR) shell G292.2−0.5 (Crawford et al. 2001). Based on Hi absorption measurements of the SNR, Caswell et al. (2004) reported a source distance of

---

ncy@physics.mcgill.ca
[1] Department of Physics, McGill University, Montreal, QC H3A 2T8, Canada
[2] School of Mathematics, University of Southampton, Southampton, SO17 1BJ, UK
[3] Jodrell Bank Centre for Astrophysics, The University of Manchester, Alan Turing Building, Manchester M13 9PL, UK
[4] Columbia Astrophysics Laboratory, Columbia University, 550 West 120th Street New York, NY 10027, USA
[5] CSIRO Astronomy and Space Sciences, Australia Telescope National Facility, Marsfield, NSW 2210, Australia
[6] Department of Physics and Astronomy, University of British Columbia, Vancouver, BC V6T 1Z1, Canada

[7] The dipole B-field can be estimated by $B = 3.2 \times 10^{19} (P\dot{P})^{1/2}$ G, where P is the spin period in second and $\dot{P}$ is the spin-down rate.

[8] Throughout this paper, we refer to rotation-powered pulsars as radio pulsars, even though their radio beams may miss the Earth, e.g. PSR J1846−0258 (Archibald et al. 2008).

[9] The braking index is defined as $n \equiv \nu\ddot{\nu}/\dot{\nu}^2$, where ν is the spin frequency and $\dot{\nu}$ and $\ddot{\nu}$ are its first and second time derivatives, respectively.

TABLE 1
X-Ray Observations of PSR J1119−6127 Used in This Study

ObsID	Date	Instrument / Mode	Net Exp.[a] (ks)
XMM-Newton			
0150790101	2003 Jun 26	PN / Large Window	41.8
		MOS1 / Full Frame	44.3
		MOS2 / Full Frame	44.8
0672790101	2011 Jun 14	PN / Large Window	27.7
		MOS1 / Full Frame	34.1
		MOS2 / Full Frame	34.3
0672790201	2011 Jun 30	PN / Large Window	27.9
		MOS1 / Full Frame	33.8
		MOS2 / Full Frame	33.7
Chandra			
2833	2002 Mar 31	ACIS-S / TE	56.8
4676	2004 Oct 31	ACIS-S / TE	60.5
6153	2004 Nov 02	ACIS-S / TE	18.9

[a] After removing periods of high background.

8.4 ± 0.4 kpc.

In the X-ray band, the pulsar and SNR were detected with *ASCA*, *ROSAT*, the *Chandra X-ray Observatory*, and *XMM-Newton* (Pivovaroff et al. 2001; Gonzalez & Safi-Harb 2003, 2005; Gonzalez et al. 2005; Safi-Harb & Kumar 2008). The pulsar emission consists of thermal and non-thermal components (Gonzalez et al. 2005; Safi-Harb & Kumar 2008) and shows strong pulsations in the soft X-ray band (Gonzalez et al. 2005). There is a faint, jet-like pulsar wind nebula (PWN) extending $7''$ from the pulsar (Gonzalez & Safi-Harb 2003; Safi-Harb & Kumar 2008), but no radio counterpart has been found (Crawford et al. 2001). The interior of SNR G292.2−0.5 shows faint, diffuse X-ray emission with spectral lines that indicate a thermal origin (Gonzalez & Safi-Harb 2005). Recently, the *Fermi Large Area Telescope* detected γ-ray pulsations from PSR J1119−6127, making it the highest B-field γ-ray pulsar yet known (Parent et al. 2011). Here we report on a detailed study of PSR J1119−6127 and SNR G292.2−0.5 using new *XMM-Newton* observations together with archival *XMM-Newton* and *Chandra* data.

2. OBSERVATIONS AND DATA REDUCTION

New observations of PSR J1119−6127 were carried out on 2011 June 14 and 30 with *XMM-Newton*. The PN camera was operated in large window mode, which has a time resolution of 48 ms, while the MOS cameras were in full-frame mode, with 2.6 s time resolution, both with the medium filter. We also reprocessed archival *XMM-Newton* and *Chandra* data taken in 2002–2004. The *Chandra* observations were all made with the ACIS-S detector, which has 3.2 s frame time. Table 1 lists the observation parameters of all data sets used in this study.

XMM-Newton data reduction was performed using SAS 11.0 with the latest calibration files. We processed the Observation Data Files with the tools `emproc/epproc`, then employed `espfilt` to remove periods of high background. The resulting exposure for the PN and MOS cameras are 97 and 112 ks, respectively. Throughout the analysis below, we used events having `PATTERN` $\leq$ `12`, unless specified otherwise. *Chandra* data reduction was carried out with CIAO 4.4 and CALDB 4.4.7. We applied the script `chandra_repro` to generate new `level=2` event files with the latest time-dependent gain, charge transfer inefficiency correction and sub-pixel adjustments. We obtained a net exposure of 136 ks after rejecting periods with background flares.

3. ANALYSIS AND RESULTS

3.1. *Imaging*

We generated individual exposure-corrected images for each PN and MOS observation with the tasks `evselect` and `eexpmap`, then combined them using `emosaic`. Figure 1 shows a three-color *XMM-Newton* image overlaid with 1.4 GHz radio contours from Crawford et al. (2001) and a broadband intensity image in the 0.3–8 keV energy range. We have also generated images with the *Chandra* data, but they are not shown here due to the poorer sensitivity and sky coverage. As shown in the figure, PSR J1119−6127 and a partial shell of SNR G292.2−0.5 are detected. The SNR emission is clumpy and it generally traces the brightest part of the $17'$ diameter radio shell, except for the diffuse emission near the pulsar, which shows no radio counterpart. The western half of the shell is brighter and redder than the eastern half. Note that the southwest rim of the shell falls outside the PN camera field of view, hence, the sensitivity is largely reduced.

3.2. *Timing*

The timing analysis was carried out with the PN data only, since only they have sufficiently high-time resolution. We extracted source events from a circular aperture of $18''$ radius centered on the pulsar. This radius was determined by the tool `eregionanalyse` to yield the optimal signal-to-noise ratio. We followed Gonzalez et al. (2005) to correct for a timing anomaly in the 2003 data; we did not find any other such anomaly in the other observations. We divided the data into low-energy (0.5–2.5 keV) and high-energy (2.5–8 keV) bands, and obtained 889 ± 30 and 414 ± 20 total counts, respectively, with ~ 110 and 120 background counts, respectively, as estimated from nearby regions. The event arrival times were first corrected to the solar system barycenter, then folded according to the radio ephemerides. We used the published pulsar ephemeris from Weltevrede et al. (2011) for the 2003 data, while the ephemeris in 2011 was obtained from contemporaneous radio observations with the Parkes radio telescope, as part of the timing program for *Fermi* (Weltevrede et al. 2010).

First, we verified that the pulse profiles in 2003 and 2011 were consistent. They were subsequently co-added in the analysis to boost the signal-to-noise ratio. The resulting profile is shown in Figure 2. The pulsar emission below 2.5 keV is highly modulated. It exhibits a single-peaked profile with good alignment with the radio pulse. A sinusoid provides an adequate fit to the profile and it gives an rms pulsed fraction (PF) of 0.38 ± 0.03. To compare with previous work, we follow Gonzalez et al. (2005) and calculate the "max–min PF" using $\mathrm{PF}=(F_{\max}-F_{\min})/(F_{\max}+F_{\min})$, where $F_{\max}$ and $F_{\min}$ are the maximum and minimum background-subtracted counts in the binned profile, respectively. In this way, we obtain max–min PF of 0.48 ± 0.12 in the 0.5–2.5 keV range. This is somewhat lower than the value 0.74 ± 0.14 reported by Gonzalez et al. (2005), and the discrepancy could be attributed to Poisson fluctuations or to difference in phase binning. On the other hand, no pulsations are detected above 2.5 keV. This is consistent with the findings of Gonzalez et al. (2005) and

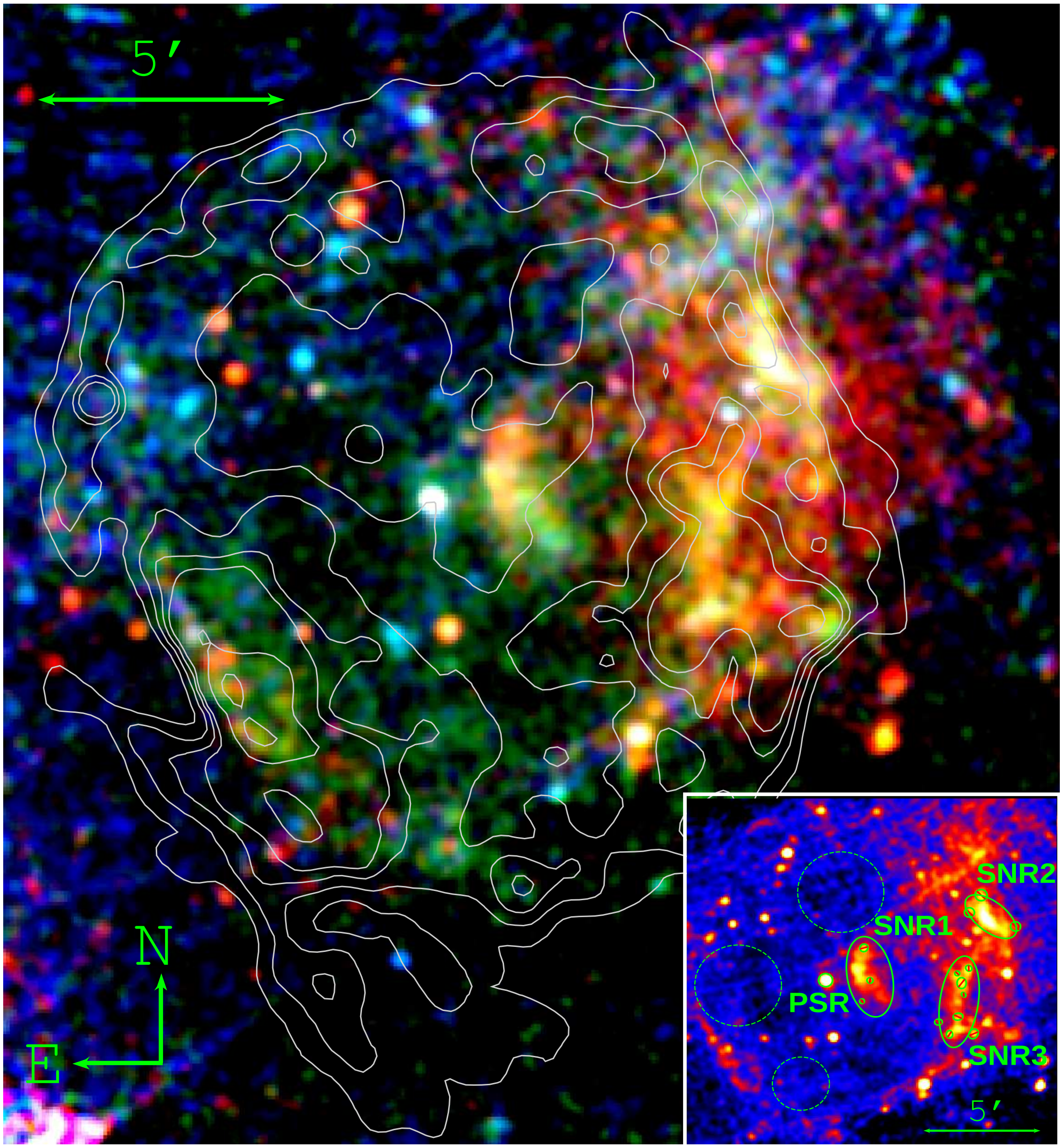

FIG. 1.— Three-color image of PSR J1119−6127 and G292.2−0.5 in the 0.3–1.5 keV (red), 1.5–3 keV (green), and 3–8 keV (blue) bands, made with all *XMM-Newton* PN and MOS data listed in Table 1 with a total exposure of 100 ks. The image is exposure-corrected, smoothed to 13″ resolution, and overlaid with 1.4-GHz radio contours from Crawford et al. (2001). Inset: intensity map in the 0.3–8 keV band, indicating the source and background extraction regions for the spectral analysis.

with the *RXTE* results in the 2–60 keV range reported by Parent et al. (2011). We place put an upper limit of PF < 10% in the 2.5–8 keV range.

3.3. *Spectroscopy*

We carried out the spectral analysis with XSPEC[10] 12.7.1. Spectra were grouped to at least 20 counts per bin, and only single and double events (i.e. `PATTERN` $\leq$ 4) were used for the PN data to ensure the best spectral calibration. We restricted the fits in the 0.5–8 keV. A photoelectric absorption model `tbabs` by Wilms et al. (2000) was employed throughout our study, and we adopted the abundances given by the same authors.

3.3.1. *Phase-averaged Pulsar Spectroscopy*

Spectra of PSR J1119−6127 were extracted from 18″-radius apertures from the *XMM-Newton* and *Chandra* data. Background spectra were extracted from nearby regions free from SNR emission shown in Figure 1. We have also tried using annular background regions centered on the pulsar, and the results are very similar. There are 1062 ± 37, 500 ± 25, 442 ± 24, and 908 ± 35 net pulsar counts in 0.5–8 keV from the PN, MOS1, MOS2, and ACIS detectors, respectively. A comparison of different spectra shows no variability between epochs. Therefore, we performed a joint fit to all the data. Given the low number of source counts, we did not attempt to account for the cross-calibration uncertainty between

---

[10] `http://heasarc.gsfc.nasa.gov/xanadu/xspec/`

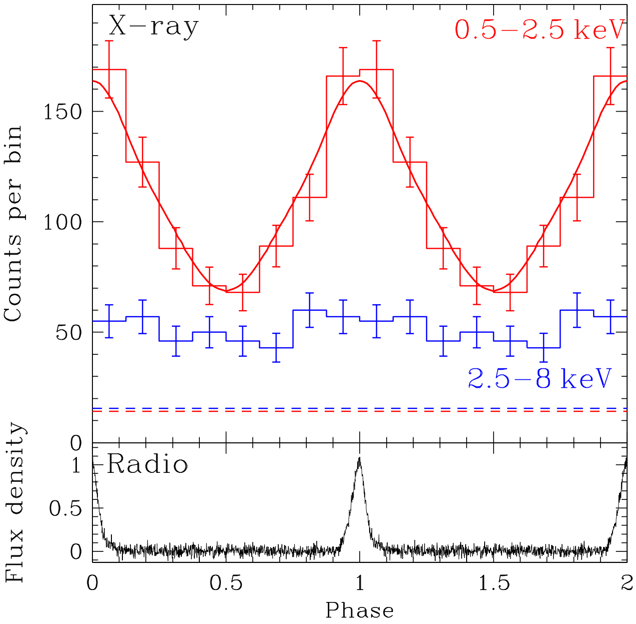

FIG. 2.— X-ray pulse profiles of PSR J1119−6127 from *XMM-Newton* PN observations in 0.5–2.5 keV (red) and 2.5–8 keV (blue). The solid line shows the model lightcurve of the soft X-ray emission from a single hot spot with a magnetized atmosphere (see Section 4.1.1). Background levels are indicated by the dashed lines. Phase 0 corresponds to the radio pulse at 1.4 GHz shown in the lower panel. The radio flux density is in an arbitrary unit.

TABLE 2
BEST-FIT BLACKBODY PLUS POWER-LAW (BB+PL) AND NEUTRON STAR ATMOSPHERE PLUS POWER-LAW (NSA+PL) MODELS TO THE PHASE-AVERAGED SPECTRUM OF PSR J1119−6127

Parameter	BB+PL	NSA^{a}+PL
$N_{\rm H}$ (10^{22} cm^{-2})	$2.2^{+0.5}_{-0.4}$	$2.5^{+0.6}_{-0.5}$
kT^{∞} (keV)	0.21 ± 0.04	$0.08^{+0.03}_{-0.02}$
R^{∞} (km)	3^{+4}_{-1}	13^{b}
Distance (kpc)	8.4^{b}	$2.4^{+5.6}_{-1.8}$
$\Gamma_{\rm PSR}$	2.1 ± 0.8	2.1 ± 0.8
$\Gamma_{\rm PWN}$	1.31^{b}	1.46^{b}
$f^{\rm abs}_{\rm bb/nsa}$ (10^{-14} erg cm^{-2} s^{-1})	1.2 ± 0.3	$1.4^{+0.2}_{-0.3}$
$f^{\rm unabs}_{\rm bb/nsa}$ (10^{-14} erg cm^{-2} s^{-1})	16^{+16}_{-7}	43^{+97}_{-25}
$f^{\rm abs}_{\rm pl}$ (10^{-14} erg cm^{-2} s^{-1})	2.3 ± 0.4	2.3 ± 0.4
$f^{\rm unabs}_{\rm pl}$ (10^{-14} erg cm^{-2} s^{-1})	5^{+6}_{-2}	5^{+5}_{-2}
$f^{\rm abs}_{\rm PWN}$ (10^{-14} erg cm^{-2} s^{-1})	2.8^{b}	2.7^{b}
$f^{\rm unabs}_{\rm PWN}$ (10^{-14} erg cm^{-2} s^{-1})	4.0^{b}	4.3^{b}
χ^2_{ν}/dof	0.97/161	0.97/161

NOTE. — All uncertainties are 90% confidence intervals (i.e., 1.6σ). $f^{\rm abs}$ and $f^{\rm unabs}$ are the absorbed and unabsorbed fluxes, respectively, in the 0.5–8 keV energy range.

[a] – A B-field strength of 10^{13} G is assumed in the NSA model.

[b] – Held fixed during the fit.

instruments (see Tsujimoto et al. 2011).

To account for the PWN contamination, we employed a PWN component in the spectral model, which was extracted from the *Chandra* data using an annular aperture of 2.5″–18″. We fitted the PWN spectrum using an absorbed power-law (PL) model with the column density ($N_{\rm H}$) fixed at the pulsar value. The PWN component was then held fixed during the fit of the pulsar spectrum. Once a new value of $N_{\rm H}$ was determined, we re-fit the PWN spectrum and the whole process was carried out iteratively until consistent spectral parameters were found. We first tried simple models, including an absorbed blackbody (BB) and an absorbed PL for the pulsar spectrum. However, they fail to describe the data, and we found that an absorbed BB+PL model provides a much better fit ($\chi^2_{\nu} = 0.97$). This gives a high effective temperature of $kT = 0.21 \pm 0.04$ keV with a emission radius of 3^{+4}_{-1} km (for a source distance of 8.4 kpc), and a PL photon index of 2.1 ± 0.8. The BB component has an absorbed flux of $1.2 \pm 0.3 \times 10^{-14}$ erg cm^{-2} s^{-1} in the 0.5–8 keV energy range, and the non-thermal components have absorbed fluxes of $2.3 \pm 0.4 \times 10^{-14}$ erg cm^{-2} s^{-1} and 2.8×10^{-14} erg cm^{-2} s^{-1} from the pulsar and the PWN, respectively. The best-fit parameters are listed in Table 2 and the PN spectrum is shown in Figure 3(a).

Following previous studies, we also tried fitting the pulsar spectra with a neutron star atmosphere model (NSA; Zavlin et al. 1996) plus a PL model. The former describes a fully ionized hydrogen atmosphere in a B-field of 10^{13} G. During the fits, the stellar mass was fixed at $1.4 M_{\odot}$ and we assumed uniform thermal emission over the entire surface of 13 km radius. This yields a fit that is equally as good as the BB+PL model, but with a significantly lower surface temperature of $0.08^{+0.03}_{-0.02}$ keV. The flux normalization suggests a distance of $2.4^{+5.6}_{-1.8}$ kpc, which is lower than the source distance of 8.4 kpc. Table 2 summarizes the best-fit parameters of the BB+PL and NSA+PL fits. All uncertainties quoted are at the 90% confidence level. The parameters are fully consistent with previous studies (Gonzalez et al. 2005; Safi-Harb & Kumar 2008), and are better constrained in our case. For the case of magnetars, BB+PL spectra are often observed (e.g., Ng et al. 2011) and the PL component is interpreted as magnetospheric upscattering of thermal photons from the surface emission (Thompson et al. 2002). To check if this is the case for PSR J1119−6127, we fitted the pulsar spectra with a resonant cyclotron scattering model (RCS; Rea et al. 2008), but obtained very poor results ($\chi^2_{\nu} \approx 2$), mainly because the model provides too little flux above 3 keV to account for the observed hard X-ray tail.

3.3.2. *Phase-resolved Pulsar Spectroscopy*

To understand the nature of the X-ray pulsations, we performed phase-resolved spectroscopy using the PN data. Based on the pulse profile in Figure 2, we extracted the off-pulse spectra from phase 0.25–0.75, and the on-pulse spectra from the rest of the phase range. There are 673 ± 29 and 385 ± 23 net counts for the on- and off-pulse emission, respectively, in the 0.5–8 keV energy range. The spectra were grouped with at least 20 counts per bin, and fitted to the BB+PL model in the 0.5–8 keV range. As shown in Figure 3(a), the pulsar emission above 2.5 keV is dominated by non-thermal emission, which shows no pulsations (see Figure 2). Therefore, the non-thermal components (from both the pulsar and the PWN) were held fixed at the phase-averaged values during the fits. We also fixed the absorption column density at the best-fit phase-averaged value of $N_{\rm H} =$

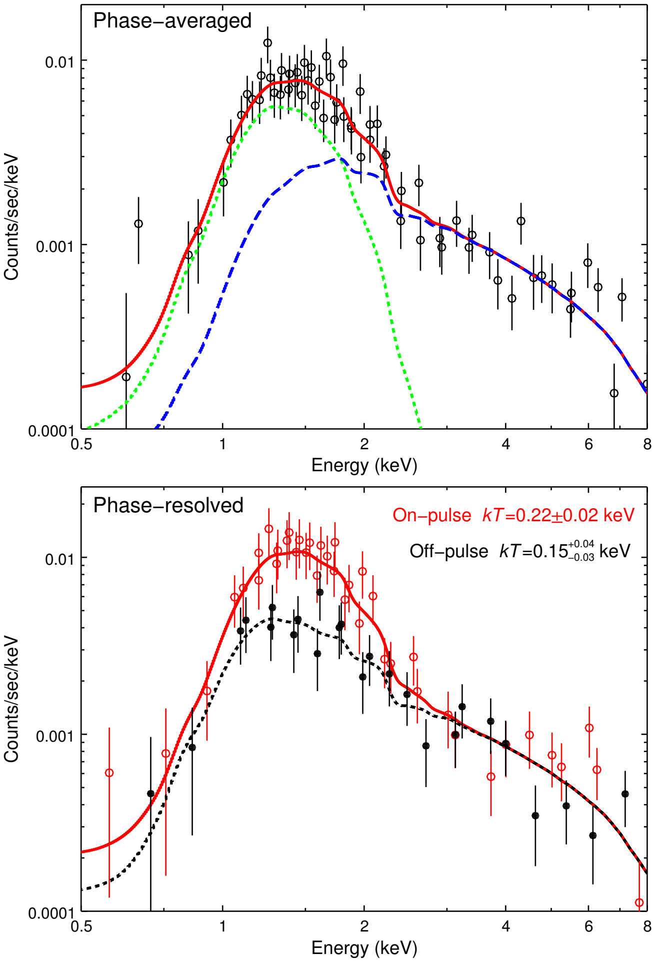

FIG. 3.— Top: best-fit blackbody plus power-law model for the phase-averaged spectrum of PSR J1119−6127. The thermal component is shown by the dotted green line and the non-thermal component, which composes of pulsar and PWN emission, is shown by the dashed blue line. Only the PN spectra are shown for clarity. Bottom: on-pulse (red open circle) and off-pulse (black filled circle) PN spectra of the pulsar, fitted with the blackbody plus power-law model. See Section 3.3.2 for details.

$2.2\times10^{22}\,\mathrm{cm}^{-2}$. We note that the non-thermal flux is not enough to account for the off-pulse emission, suggesting the presence of thermal emission at pulse minimum. We found a higher BB temperature of $kT = 0.22 \pm 0.02\,\mathrm{keV}$ with an effective radius of $R = 3.0^{+1.0}_{-0.8}\,\mathrm{km}$ for the on-pulse emission. The off-pulse emission shows a hint of a lower temperature of $kT = 0.15^{+0.04}_{-0.03}\,\mathrm{keV}$ and a larger radius of $7^{+13}_{-7}\,\mathrm{km}$. The best-fit spectral models are shown in Figure 3(b). We have also tried fitting the difference spectrum between on- and off-pulse emission. While it is consistent with a BB model, there are large uncertainties in the spectral parameters due to poor data quality.

3.3.3. *SNR Spectroscopy*

We extracted spectra of SNR G292.2−0.5 from the three brightest regions (see Figure 1) from the *XMM-Newton* and *Chandra* data. Our region 1 roughly corresponds to the "east" region in Gonzalez & Safi-Harb (2005), and regions 2 and 3 correspond to their "west" region. Point sources inside these regions were identified and excluded based on the exposure-corrected *Chandra* and *XMM-Newton* images. We note that region 2 is not covered by any *Chandra* observations, therefore, only the *XMM-Newton* spectra are used in this case. Similarly, only one *Chandra* exposure is useful for region 3. Since the SNR covers a large part of the *Chandra* and *XMM-Newton* PN field of view, we estimated the background spectra using the blank-sky data provided by the calibration teams (Carter & Read 2007), which were taken from nearby regions in the Galactic plane. We also tried extracting the background spectra from source-free regions far off-axis in our observations and obtained similar results, although this way the sky background tends to be underestimated due to vignetting. After background subtraction, we obtained 1.1×10^4 *XMM-Newton* counts and 5300 *Chandra* counts for region 1, 4900 *XMM-Newton* counts for region 2, and 7900 *XMM-Newton* counts and 2000 *Chandra* counts for region 3 in 0.5–7.5 keV range.

Emission lines are found in all the spectra, albeit rather weak, indicating a thermal origin for the emission. For each region, we performed a joint fit to the spectra with all parameters linked, and we introduced a constant scaling factor between the *XMM-Newton* and *Chandra* spectra to account for the cross-calibration uncertainty (Tsujimoto et al. 2011). We first tried the spectral parameters reported by Gonzalez & Safi-Harb (2005), but these gave very poor fits. Using a non-equilibrium ionization thermal model (PSHOCK; Borkowski et al. 2001) with solar abundances, we obtained reasonable results (χ^2_ν =1.3–1.5). The fits can be further improved by allowing the abundances to vary (with the VPSHOCK model) or by adding a hard component, and the improvements are statistically significant as indicated by F-tests. However, since the emission lines are weak, the VPSHOCK fits require rather low abundances (0.1–0.5) for all elements between Ne and Fe. Therefore, we believe that a two-component model could be a more physical description of the thermal emission. In this case, the hard component can be described by either a non-thermal PL with photon indices Γ = 2.9–3.5 or by a high temperature (kT = 1–1.8 keV) PSHOCK model with very low ionization timescales ($\tau \lesssim 10^9\,\mathrm{s\,cm^{-3}}$) and solar abundances, and they provide the best fits overall ($\chi^2_\nu \approx$1.2). The results are listed in Table 3 and the best-fit two-temperature models are plotted in Figure 4. In all the fits, the soft component has a large ionization timescales ($\tau \gtrsim 10^{12}\,\mathrm{s\,cm^{-3}}$). The *Chandra* flux is ∼ 30% higher than the *XMM-Newton* flux, which is not atypical (see Tsujimoto et al. 2011).

4. DISCUSSION

In the following discussion, we adopt a source distance of 8.4 kpc and an age of 1.9 kyr. Although the true age of the system could be different than the pulsar's characteristic age, we stress that our discussion should remain qualitatively valid for a system age younger than a few thousand years.

4.1. *PSR J1119−6127*

4.1.1. *Thermal Emission*

PSR J1119−6127 is among the youngest radio pulsars with thermal emission detected. As indicated in Figure 3(a), the pulsar flux below 2.5 keV is mostly thermal, and it is highly pulsed and shows good phase align-

TABLE 3
Best-fit PSHOCK Plus Power-law (PS+PL) and Two-temperature PSHOCK (PS+PS) Models for the Spectra of SNR G292.2−0.5

Parameter	Region 1		Region 2		Region 3	
	PS+PL	PS+PS	PS+PL	PS+PS	PS+PL	PS+PS
$N_{\rm H}$ ($10^{22}\,{\rm cm^{-2}}$)	$2.17^{+0.07}_{-0.08}$	$2.17^{+0.10}_{-0.08}$	$1.9^{+0.5}_{-0.2}$	0.9 ± 0.2	$1.15^{+0.07}_{-0.03}$	1.0 ± 0.1
kT_1 (keV)	0.18 ± 0.02	$0.18^{+0.3}_{-0.2}$	$0.11^{+0.05}_{-0.02}$	$0.74^{+0.11}_{-0.03}$	$0.66^{+0.03}_{-0.02}$	0.66 ± 0.03
τ_1 ($10^{10}\,{\rm s\,cm^{-3}}$)	40^{+40}_{-20}	90^{+90}_{-40}	> 150	> 30	> 200	> 100
${\rm EM}_1$ ($10^{56}\,{\rm cm^{-3}}$)	360^{+200}_{-140}	330^{+160}_{-120}	1100^{+3000}_{-400}	0.5 ± 0.2	$1.9^{+0.4}_{-0.5}$	$1.5^{+0.6}_{-0.4}$
Γ	2.9 ± 0.1	$\cdots$	$3.5^{+0.2}_{-0.1}$	$\cdots$	3.5 ± 0.2	$\cdots$
kT_2 (keV)	$\cdots$	$1.8^{+0.2}_{-0.1}$	$\cdots$	1.8 ± 0.2	$\cdots$	1.0 ± 0.1
τ_2 ($10^{10}\,{\rm s\,cm^{-3}}$)	$\cdots$	< 0.2	$\cdots$	< 0.08	$\cdots$	< 0.08
${\rm EM}_2$ ($10^{56}\,{\rm cm^{-3}}$)	$\cdots$	$4.2^{+0.4}_{-0.6}$	$\cdots$	2.2 ± 0.3	$\cdots$	$4.2^{+0.8}_{-0.7}$
$f_1^{\rm abs}$	0.64 ± 0.03	0.45 ± 0.02	$0.15^{+0.04}_{-0.03}$	$0.22^{+0.07}_{-0.06}$	0.51 ± 0.08	$0.48^{+0.09}_{-0.08}$
$f_1^{\rm unabs}$	330^{+100}_{-80}	300^{+110}_{-80}	330^{+700}_{-150}	$1.1^{+0.8}_{-0.5}$	$3.5^{+0.9}_{-0.8}$	$2.9^{+1.0}_{-0.8}$
$f_2^{\rm abs}$	1.46 ± 0.06	$1.3^{+0.07}_{-0.05}$	1.5 ± 0.05	0.88 ± 0.08	$0.73^{+0.10}_{-0.09}$	$0.72^{+0.08}_{-0.09}$
$f_2^{\rm unabs}$	$6^{+0.6}_{-0.5}$	7^{+7}_{-4}	6^{+2}_{-1}	$1.8^{+0.9}_{-0.1}$	3.7 ± 0.7	$2.1^{+1.8}_{-0.2}$
χ^2_ν/dof	1.21/1175	1.21/1174	1.19/363	1.18/362	1.35/782	1.31/781

Note. — The subscripts 1 and 2 correspond to the soft and hard components, respectively. All uncertainties are 90% confidence intervals (i.e. 1.6σ). The volume emission measure is given by ${\rm EM} = \int n_e n_{\rm H}\,{\rm d}V$, where n_e and $n_{\rm H}$ are shocked electron and hydrogen number densities, respectively. $\tau = n_e t$ is the ionization timescale. The absorbed and unabsorbed fluxes ($f^{\rm abs}$ and $f^{\rm unabs}$) are estimated from the *XMM-Newton* data, in units of $10^{-13}\,{\rm erg\,cm^{-2}\,s^{-1}}$ in the 0.5–8 keV energy range.

ment with the radio pulse (Figure 2). Combining these two results suggests that the thermal emission could be dominated by a single hot spot near the magnetic pole. Further support for this picture is provided by the phase-resolved spectroscopy, which suggests a hint of a higher temperature for the on-pulse emission than the off-pulse emission (Figure 3(b)). The BB+PL fit to the phase-averaged spectrum gives a high temperature of 0.21 ± 0.04 keV ($= 2.4 \pm 0.5$ MK) with an emission radius of 3^{+4}_{-1} km, implying a bolometric luminosity of $1.9^{+1.9}_{-0.8} \times 10^{33}\,{\rm erg\,s^{-1}}$ for the thermal emission. The BB temperature and luminosity are among the highest of radio pulsars, even when compared to objects with similar age (see Olausen et al. 2010; Ng & Kaspi 2011; Zhu et al. 2011). Since the stellar surface temperature is non-uniform, the NSA fits only give the average temperature and it cannot be directly compared to the BB temperature. Indeed, the bolometric luminosity above is equivalent to that of a 13 km radius star with a uniform temperature of 0.096 keV (=1.1 MK), comparable to the best-fit NSA temperature of $0.08^{+0.03}_{-0.02}$ keV.

Gonzalez et al. (2005) and Safi-Harb & Kumar (2008) pointed out that the BB luminosity and radius are too large to be reconciled with polar cap heating by return currents from the magnetosphere. Hence, the thermal emission is likely from cooling and its unusual properties, e.g. high temperature and large modulation, could be related to the strong magnetic field of PSR J1119−6127. Pons et al. (2007) noticed an apparent correlation between the BB temperature T and the dipole B-field B_d of neutron stars, with $T \propto \sqrt{B_d}$ spanning over three orders of magnitude in B_d, from radio pulsars to magnetars. They attributed this to crustal heating by magnetic field decay, and subsequently studied the "magneto-thermal evolution" of neutron stars (Aguilera et al. 2008a,b; Pons et al. 2009). In their model, heating from field decay increases the magnetic diffusivity and thermal conductivity of the crust, which in turn accelerates the field decay. As a result, neutron stars born with initial B-fields $> 5 \times 10^{13}$ G could have a surface temperature well above the minimal cooling scenario (Aguilera et al. 2008a; Kaminker et al. 2009).

The thermal emission of PSR J1119−6127 offers an interesting test case for the above theory. While the BB temperature we obtained is comparable to the predicted value at the pole (Aguilera et al. 2008a), the bolometric luminosity of $\sim 10^{33} - 10^{34}\,{\rm erg\,s^{-1}}$ could be easily explained by passive cooling (e.g. Page et al. 2004), thus, providing no evidence for energy injection from B-field decay. Indeed, the higher temperature at the pole could be attributed to anisotropic heat conduction. Since free electrons, which are the main heat carriers, are confined to the magnetic field lines, heat transport perpendicular to the field is strongly suppressed (Greenstein & Hartke 1983). This acts as a "heat blanket" at the magnetic equator, while the magnetic poles are in thermal equilibrium with the core. As a result, the surface temperature distribution is non-uniform with warmer spots at the magnetic poles separated by cooler regions at lower magnetic latitude (e.g. Geppert et al. 2004; Shabaltas & Lai 2012).

It is believed that the internal magnetic field of a neutron star likely consists of a toroidal component, which could be generated by differential rotation that wraps the poloidal field in a proto-neutron star (e.g. Thompson & Duncan 1993). Geppert et al. (2006) showed that the presence of a toroidal B-field in the crust could further suppress the heat transport from the core towards the magnetar equator, because that requires crossing the toroidal field lines. As a result, this would enhance the heat blanket effect. Moreover, since the toroidal field component is symmetric about the magnetic equator but the poloidal component is antisymmet-

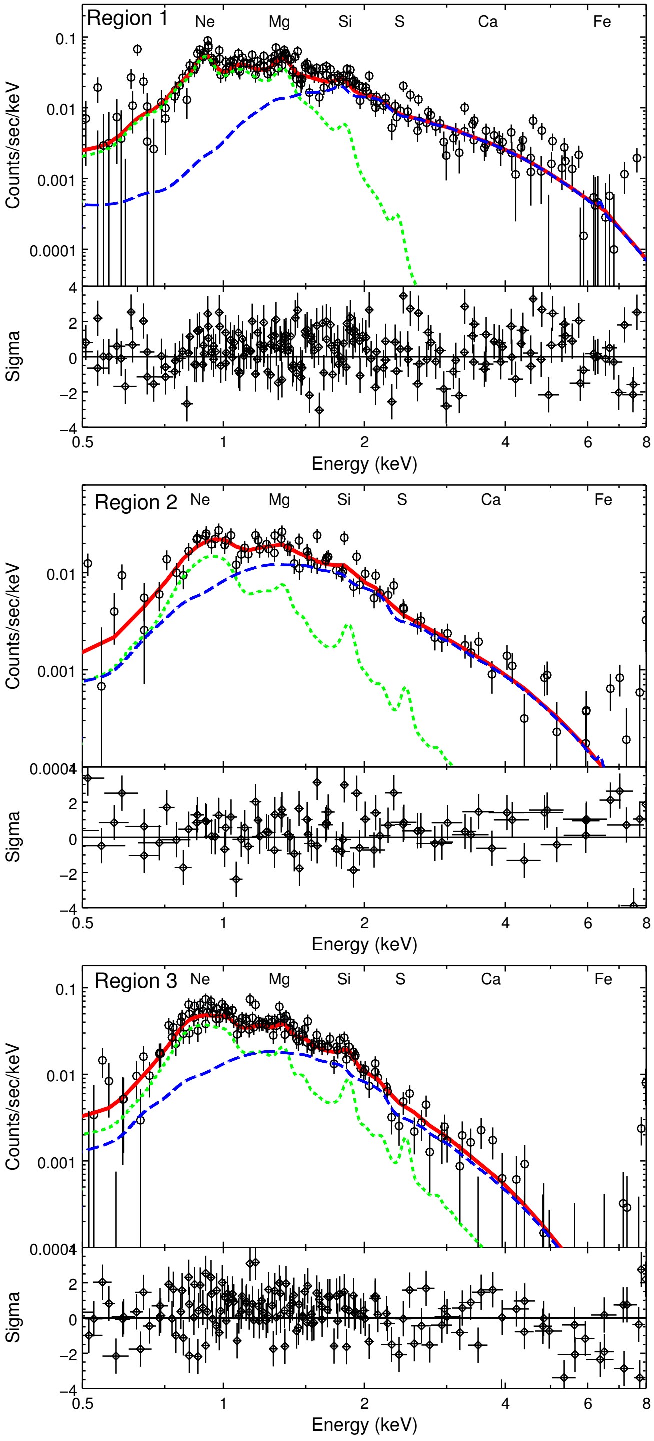

FIG. 4.— Best-fit two-temperature PSHOCK models to the spectra of SNR G292.2−0.5. The high- and low-temperature components are indicated by the dashed blue lines and dotted green lines, respectively. For clarity, only the PN spectra are shown and all spectra are grouped with a minimum of 50 counts per bin.

ric, the total B-field would be asymmetric. Hence, the thermal emission from one magnetic pole could dominate over another, which could help explain the single-peaked pulse profile we found. Furthermore, the PF could be boosted by effects of limb-darkening and magnetic beaming in the neutron star atmosphere (e.g., Pavlov et al. 1994; Rajagopal et al. 1997; van Adelsberg & Lai 2006). Magnetic beaming is due to anisotropic scattering and absorption of photons in magnetized plasmas. The resulting radiation from a hot spot consists of a narrow pencil beam $< 5°$ along the magnetic field and a broad fan beam at intermediate angles of 20°–60° (Zavlin et al. 1995; van Adelsberg & Lai 2006).

To test these ideas, we employed a magnetized partially ionized hydrogen atmosphere model (Ho et al. 2008), which accounts for the magnetic and relativistic effects, to generate X-ray spectra and pulse profiles with a similar procedure as Ho (2007). We took a surface B-field of 4×10^{13} G and surface redshift of $1 + z = 1.19$, and adopted the viewing geometry of magnetic inclination angle $\alpha \approx 125°$ and spin-axis inclination angle $\zeta \approx 145°$ obtained from modeling of the pulsar γ-ray lightcurve and radio polarization profile (Parent et al. 2011). Vacuum polarization is ignored here, since it is not important for the total surface emission at this field strength (van Adelsberg & Lai 2006). We tried different model parameters and found that two identical antipodal hot spots give a very low PF of $\sim 5\%$. The observed single-peaked pulse profile can be produced if the temperature of one hot spot is higher than the other. Our best-fit model is given by a hot spot with effective temperature (observed at infinity) of $kT = 0.13\,\mathrm{keV}$ (i.e. 1.5 MK) and an area of one third of the stellar surface, and for the other hot spot, we place a temperature upper limit of 0.08 keV assuming a similar area. This is shown by the solid line in Figure 2. This temperature is lower than the best-fit BB temperature for the on-pulse spectrum (see Figure 3(b)) and also the emitting area here is larger. These are typical characteristics of an atmosphere model when compared to a simple BB, since non-gray opacities in the former cause higher energy photons to be seen from deeper and hence hotter layers in the atmosphere (e.g. Romani 1987; Shibanov et al. 1992). Note that the model suggests a rather large emitting area. This is because given the viewing geometry, the observer's line of sight would cut through the fan beam twice during one rotation. Therefore, a much smaller hot spot would produce a double-peaked pulse profile. Finally, our model predicts a decreasing "max–min PF" with energy, from 0.5 at 0.5 keV to 0.4 at 2 keV, however, this difference is too small to be detected given our data quality. Deeper observations are needed to confirm this.

As a caveat, we note that the viewing geometry obtained from the γ-ray lightcurve is model dependent. If the constraints on α and ζ are relaxed, the high PF could also be explained by some extreme viewing geometries, such that only one pole is observable (see Gonzalez et al. 2005).

4.1.2. *Non-thermal Emission*

The X-ray spectrum of PSR J1119−6127 clearly shows a PL component with a photon index of $\Gamma = 2.1 \pm 0.8$ and an unabsorbed flux of $5^{+6}_{-2} \times 10^{-14}\,\mathrm{erg\,cm^{-2}\,s^{-1}}$ in the 0.5–8 keV range. Since the RCS model gives a poor fit, this seems unlikely to be up-scattering of thermal photons as in magnetars. We believe that it could be synchrotron radiation originated from the PWN or from the pulsar magnetosphere. Assuming constant surface brightness, the PWN would provide an unabsorbed flux of only $8 \times 10^{-16}\,\mathrm{erg\,cm^{-2}\,s^{-1}}$ in the 0.5–8 keV range

TABLE 4
High-B Radio Pulsars with Detected Pulsed Thermal Emission

Name	P (s)	B (10^{13} G)	τ_c (kyr)	Distance (kpc)	kT (keV)	$L_{\rm bol}$ ($10^{32}\,{\rm erg\,s^{-1}}$)	PF	Reference
J1119−6127	0.41	4.1	1.7	8.4	0.21 ± 0.04	19^{+19}_{-8}	0.48 ± 0.12	This work
J1819−1458	4.3	5.0	117	∼3.6	0.12 ± 0.02	$1.2^{+2}_{-0.8}$	0.37 ± 0.05	1
J1718−3718	3.4	7.4	34	∼4.5	0.19 ± 0.02	4^{+5}_{-2}	0.60 ± 0.13	2

References. — (1) Rea et al. 2009; (2) Zhu et al. 2011.

Note. — The characteristic ages (τ_c) are inferred from the spin parameters. kT are the best-fit blackbody temperatures. The pulsed fractions (PF) are estimated with the "max–min PF" (see the text) in 0.5–2.5 keV, 0.3–5 keV, and 0.8–2 keV for PSRs J1119−6127, J1819−1458, and J1718−3718, respectively.

in the central $2\farcs5$-radius region. However, the actual PWN contribution is likely to be higher, since compact PWN emission is often found to be peaked toward the pulsar (see Ng & Romani 2008). Deeper *Chandra* observations are needed to determine if the PL photon indices of the pulsar and PWN components are consistent. In addition to PWN emission, young rotation-powered pulsars generally show strong magnetospheric emission in X-rays (e.g. Ng et al. 2008a). However, this emission is expected to be highly pulsed (Zhang & Cheng 2002), which is not observed in our case. At a distance of 8.4 kpc, the non-thermal emission we found has a luminosity of $L_X = 4.2 \times 10^{32}\,{\rm erg\,s^{-1}}$ (0.5–8 keV), a few times larger than the flux $8.5 \times 10^{31}\,{\rm erg\,s^{-1}}$ suggested by Zhang & Jiang (2005) based on the outergap model.

4.1.3. *Connection with Other High-B Pulsars and Magnetars*

Among all high-B radio pulsars listed in Ng & Kaspi (2011), only four (PSRs J1119−6127, J1819−1458, J1718−3718, and J1846−0258) are bright enough to have X-ray pulsations detected. Except PSR J1846−0258, which has a purely non-thermal spectrum (Gotthelf et al. 2000; Ng et al. 2008a), the rest show thermal emission with high BB temperature around 0.1–0.2 keV. We summarize their timing and spectral properties in Table 4. Interestingly, their X-ray pulse profiles are all single-peaked and well aligned with the radio pulse, and show large modulations with PFs from 40% to 60%. These striking similarities suggest that the physics we discussed above in Section 4.1.1 could be applicable to other high-B pulsars. More X-ray observations are needed to confirm this idea. In particular, PSRs J1734−3333 and B1916+14, which are detected in X-rays but for which no pulsations have yet been found (Olausen et al. 2012; Zhu et al. 2009; Olausen et al. 2010), would be ideal targets.

PSR J1846−0258 is a very special object in the class, as it has shown magnetar-like activity, including short X-ray bursts (Gavriil et al. 2008) accompanied by a glitch with unusual recovery properties (Livingstone et al. 2010, 2011). This led to speculation that high-B radio pulsars could be magnetars in quiescence. It has been proposed that radio pulsars and magnetars could be a unified class of objects (Kaspi & McLaughlin 2005; Perna & Pons 2011) and high-B pulsars could exhibit magnetar-like bursting behavior, albeit less frequently (∼1 per century). Radio timing of PSR J1119−6127 revealed a glitch in 2007 that induced abnormal radio emission (Weltevrede et al. 2011). It is unclear if the pulsar exhibited any X-ray variability at the same time, due to the lack of sensitive X-ray monitoring. Our *XMM-Newton* observations in 2011 are not useful, since the post-outburst flux relaxation timescale is likely shorter than a few years (e.g. Livingstone et al. 2011). This highlights the importance of X-ray monitoring or rapid post-glitch follow-up in the study of high-B radio pulsars and magnetars.

4.2. *SNR G292.2−0.5*

4.2.1. *SNR Environment and Evolution*

We have carried out spectral analysis of three brightest regions in SNR G292.2−0.5. The spectra are well-described by absorbed two-component models. While the best-fit absorption column densities of the pulsar and region 1 are consistent ($\sim 2 \times 10^{22}\,{\rm cm^{-2}}$), the values are lower for regions 2 and 3 ($\sim 1 \times 10^{22}\,{\rm cm^{-2}}$). These seem to suggest an east-west gradient of $N_{\rm H}$ across the field. This is more evident in the three-color image in Figure 1: the western part of the SNR is redder than the eastern part, indicating a softer spectrum which could be due to a lower absorption. This trend is consistent with previous findings (Pivovaroff et al. 2001; Gonzalez & Safi-Harb 2005; Gonzalez et al. 2005; Safi-Harb & Kumar 2008), and can be attributed to a dark molecular cloud DC 292.3−0.4 to the east of the pulsar as first proposed by Pivovaroff et al. (2001).

The SNR emission consists of a soft thermal component with $kT < 1$ keV and a hard component that can be described either by a non-thermal PL of photon index $\Gamma = 2.9-3.5$ or by high temperature non-equilibrium ionization plasma with $kT = 1-2$ keV. While non-thermal synchrotron emission is often observed in young SNRs, the PL photon index we found ($\Gamma \sim 3.5$) is higher than the typical values of 2–3 in other systems (see a review by Reynolds 2008). In addition, the fit statistics are slightly worse than that of the two-temperature model. These seem to suggest that the latter may be a more plausible model. In this case, the solar abundances of the high-temperature plasma suggest a circumstellar or interstellar origin, hence, the reverse shock probably has not yet propagated through the ejecta. Together with the high temperature and small ionization timescales, these provide support for the young age of the system. The emission measure could give us a handle on the ambient density n_0. Assuming a slab geometry for the emitting regions with thickness equal to the width, and taking an electron-to-proton density ratio of 1.2 and a shock compression ratio of 4, we obtained $n_0 \sim 0.1\,\mathrm{cm}^{-3}$ in all three regions. The low-temperature component, however, is more difficult to interpret. Following the same calculation, we estimate n_0 of 0.6, 0.03, and $0.07\,\mathrm{cm}^{-3}$ in regions 1, 2, and 3, respectively. This could suggest dense clump for region 1. For regions 2 and 3, a comparison to the large ionization timescales ($\tau \gtrsim 10^{12}\,\mathrm{s\,cm}^{-3}$) indicates that the plasma could have been shocked $\sim 10^5\,\mathrm{yr}$ ago, which seems difficult to reconcile with the SNR emission. As we suggest below, the emission may arise from the progenitor wind interaction with the surrounding.

At a distance of 8.4 kpc, the $8\overset{\prime}{.}5$-radius SNR shell has a physical size of 21 pc (Caswell et al. 2004). Such a large radius at a young age requires a high average expansion rate of $v_s = 21\,\mathrm{pc}/1.9\,\mathrm{kyr} = 1.1\times10^4\,\mathrm{km\,s}^{-1}$. If this is the present-day shock velocity, then the proton temperature would be $kT_p = 0.11 m_\mathrm{H} v_s^2 = 130\,\mathrm{keV}$, where m_H is the proton mass, and an adiabatic index of $\gamma = 5/3$ and cosmic abundances (i.e., 90% H and 10% He) are assumed. A comparison to the best-fit $kT \approx 1\,\mathrm{keV}$ implies an electron-to-proton temperature ratio of ~ 0.01, lower than in most SNRs observed (see van Adelsberg et al. 2008). If the ambient medium has a uniform density of $n_0 \approx 0.1\,\mathrm{cm}^{-3}$ as estimated above, then the swept-up mass would be $\sim 100\,M_\odot$, much larger than the typical ejecta mass of $\lesssim 10 M_\odot$. Hence, the remnant could be in a transition to the adiabatic phase. Based on the Sedov solution, Crawford et al. (2001) derived a constraint on the ratio between n_0 (in cm^{-3}) and the explosion energy E_{51} in units of 10^{51} erg. The updated distance and age estimates from Caswell et al. (2004) and Weltevrede et al. (2011) imply $E_{51}/n_0 = 200$, requiring an exceptionally large explosion energy or a very low ambient density. It has been proposed that a newborn neutron star with magnetar-like B-field ($\sim 10^{15}$ G) and a short spin period (~ 1 ms) would spin down quickly via magnetic braking. As a result, the huge amount of rotational energy released ($\sim 10^{52}$ erg) could accelerate the SNR expansion (Allen & Horvath 2004). While we cannot rule out this possibility, the explosion energies of three SNRs associated with magnetars (Kes 73, CTB 109, and N49) are found to be close to the canonical value of 10^{51} erg (Vink & Kuiper 2006), which is not consistent with this hypothesis.

As an alternative, the supernova could have occurred in a low-density wind bubble (e.g., Gaensler et al. 1999; Gvaramadze 2006; Ng et al. 2007). This scenario was briefly mentioned by Caswell et al. (2004) and here we further explore this idea. Chevalier (2005) discussed different types of core collapse supernovae and the properties of their remnants. Type IIP and IIL/b supernovae are the end products of red supergiants (RSGs), which have initial masses $\sim 9-25 M_\odot$ and $\sim 25-35 M_\odot$, respectively (Heger et al. 2003), and they are surrounded by dense circumstellar RSG winds extending to a few pc. In contrast, supernovae of Type Ib/c are believed to originate from Wolf-Rayet (WR) progenitors, which are massive stars $\gtrsim 35 M_\odot$ with high mass-loss rates and high-velocity winds, which are about two orders of magnitudes faster than RSG winds. For a WR star evolved from an RSG, the fast WR wind would sweep up the slow RSG wind ejected earlier to evacuate a low-density wind bubble of radius $\gtrsim 10$ pc over the lifetime $\sim 2\times10^5$ yr of the WR phase (Chevalier 2005). The swept-up shell is characterized by clumpy structure due to Rayleigh-Taylor instabilities, and overabundance in N and underabundance in C and O (Garcia-Segura et al. 1996).

We argue that SNR G292.2−0.5 is unlikely to be a Type IIP or IIL/b supernova because in these cases the remnant should expand into the dense circumstellar RSG winds. A Type Ib/c event with a WR progenitor, one of the possibilities mentioned by Chevalier (2005), therefore seems more likely. In this picture, the SNR had a long free-expansion phase in the low-density wind bubble, with the initial expansion rate up to a few times $10^4\,\mathrm{km\,s}^{-1}$, as seen in SN 1987A (Gaensler et al. 1997; Ng et al. 2008b). When the shock reached the cavity boundary at large radius, it began to encounter the clumpy swept-up shell and hence decelerated. The shock interaction then gave rise to the observed hard component in the spectra, either thermal or non-thermal. This scenario may be able to explain the soft component too. The large ionization timescales of the emission are comparable to the lifetime of the WR phase, suggesting that it may originate from the swept-up RSG wind. Two WR bubbles have been detected in X-rays and their spectra can be fitted by a two-temperature thermal model with $kT \sim 0.1$ and 1 keV (Wrigge et al. 2005; Toalá et al. 2012). The high-temperature component is comparable to what we observed for SNR G292.2−0.5, while the low-temperature component may be too absorbed to detect in our case. In addition, hydrodynamic simulations and observations suggest a density of $\sim 0.1\,\mathrm{cm}^{-3}$ in the hot bubbles (Garcia-Segura et al. 1996; Dwarkadas 2007; Toalá et al. 2012), which is also consistent with our findings. Deeper X-ray observations in the future can probe the chemical composition of the circumstellar medium to confirm its nature. Moreover, if the SNR is detected in optical wavelengths, then spectral line observations could directly measure the shock velocity to reveal the evolutionary state of the remnant.

4.2.2. *Progenitors of High-B Pulsars and Magnetars*

In addition to PSR J1119−6127, only two other young high-B radio pulsars have associated SNRs detected: PSR J1846−0258 in Kes 75 and PSR B1509−58 in MSH 15−5*2*. Intriguingly, both of them were claimed to have a WR progenitor (Morton et al. 2007; Gaensler et al. 1999). There is also observational evidence hinting at a similar mass range for magnetar progenitors, e.g., 1E 1048.1−5937, CXOU J1647−4552, and SGR 1806−20 (Gaensler et al. 2005; Muno et al. 2006; Figer et al. 2005), although intermediate masses were suggested for two cases: 1E 1841−045 and SGR 1900+14 (Chevalier 2005; Davies et al. 2009). This raises the important question regarding a possible correlation between progenitor mass and neutron star magnetic field. Recently, Chevalier (2011) compared different classes of young neutron stars in SNRs, including magnetars, radio pulsars, and central compact objects, and suggested a tendency for higher B-field objects to have more massive progenitors. However, it was noted that other parameters, such as rotation, metallicity, and binarity, likely also play an important role.

The origin of magnetic fields in neutron stars has long been an open problem. Theories suggest that it could be the fossil B-fields of the progenitors preserved during core collapse (e.g., Woltjer 1964; Ruderman 1972; Ferrario & Wickramasinghe 2006) or from field amplification via an α–Ω dynamo in rapidly rotating stars (e.g., Duncan & Thompson 1992; Thompson & Duncan 1993). A positive correlation between progenitor mass and neutron star B-field may be expected in both scenarios (Ferrario & Wickramasinghe 2008). Massive stars tend to have higher surface B-fields (Petit et al. 2008). They also spend less time in the hydrogen and helium burning phases, during which significant braking occurs. Hence, the core could retain a large angular momentum, resulting in efficient dynamo action. If further studies confirm that the progenitors of high-B radio pulsars and magnetars have comparable mass, then no matter which of the above mechanisms is at work, the B-fields in these objects could be generated in a similar way. In this respect, magnetars could have the same formation channel as radio pulsars, which would support a unification of these classes of objects (Kaspi & McLaughlin 2005; Kaspi 2010; Perna & Pons 2011).

5. CONCLUSION

We performed a detailed X-ray study of the young high-B radio pulsar J1119−6127 and its associated SNR G292.2−0.5 using deep *XMM-Newton* and *Chandra* observations. The pulsar emission exhibits strong pulsations below 2.5 keV, with a single-peaked profile that aligns with the radio pulse. Such a single-peaked profile and alignment seem common among thermally emitting high-B pulsars, and we showed that the observed pulsed profile can be modeled by a large hot spot near the magnetic pole. The pulsar spectrum is well fitted by an absorbed BB plus PL model. The BB temperature $kT = 0.21 \pm 0.04\,\mathrm{keV}$ is highest among young radio pulsars. The thermal emission has a bolometric luminosity of $1.9^{+1.9}_{-0.8} \times 10^{33}\,\mathrm{erg\,s^{-1}}$, which is consistent with neutron star cooling and no heating by B-field decay is needed. However, passive magnetic effects, including anisotropic heat conduction and beaming, must play a part in the high temperature and large modulation of the emission.

The spectra of SNR G292.2−0.5 are best fitted by a two-component model with solar abundances. The soft component has a thermal origin with $kT \lesssim 1\,\mathrm{keV}$ and a large ionization timescale, while the hard component can be described either by a PL with $\Gamma = 2.9 - 3.5$ or by higher temperature ($kT = 1 - 2\,\mathrm{keV}$) thermal emission with low ionization. For a young age of 1900 yr inferred from the pulsar's spin down, the 21 pc SNR shell diameter (at a distance of 8.4 kpc) implies a fast expansion in the past. This could be the result of exceptionally large explosion energy $\gtrsim 10^{52}$ erg or supernova in a wind cavity. We believe that the latter is more plausible, and this could suggest a Type I b/c supernova with a WR progenitor. WR stars have a typical mass $\gtrsim 35\,M_\odot$ and they have also been proposed as the progenitors for two other high-B radio pulsars. There is evidence that magnetar progenitors could be in a similar mass range, leading to a speculation that the two classes of neutron stars may have the same formation channel. If confirmed, it will provide a strong support to the idea of unification of these classes of objects.

We note that late in the preparation of this manuscript, we became aware of work (Kumar et al. 2012) on the study of the SNR using the same archival *Chandra* data and a subset (~ 50 ks) of *XMM-Newton* data we have used in our study. While our deeper observations gave different spectral parameters for SNR G292.2−0.5, we arrived at similar conclusions regarding a possible massive progenitor for PSR J1119−6127.

Facilities: CXO (ACIS) *XMM* (EPIC)

We thank Bryan Gaensler for providing the radio image, and we thank Pat Slane and Daniel Castro for useful discussions. We also thank the referee for useful comments. This work was based on observations obtained with *XMM-Newton*, an ESA science mission with instruments and contributions directly funded by ESA Member States and NASA. This research has made use of the NASA Astrophysics Data System (ADS) and software provided by the Chandra X-ray Center (CXC) in the application package CIAO. V.M.K. holds the Lorne Trottier Chair in Astrophysics and Cosmology and a Canadian Research Chair in Observational Astrophysics. This work is supported by NSERC via a Discovery Grant, by FQRNT via the Centre de Recherche Astrophysique du Quebec, by CIFAR, and a Killam Research Fellowship. W.C.G.H. appreciates the use of the computer facilities at the Kavli Institute for Particle Astrophysics and Cosmology, and acknowledges support from the Science and Technology Facilities Council (STFC) in the United Kingdom.

REFERENCES

Aguilera, D. N., Pons, J. A., & Miralles, J. A. 2008a, A&A, 486, 255
Aguilera, D. N., Pons, J. A., & Miralles, J. A. 2008b, ApJ, 673, L167
Allen, M. P., & Horvath, J. E. 2004, ApJ, 616, 346
Archibald, A. M., Kaspi, V. M., Livingstone, M. A., & McLaughlin, M. A. 2008, ApJ, 688, 550
Borkowski, K. J., Lyerly, W. J., & Reynolds, S. P. 2001, ApJ, 548, 820
Camilo, F., Kaspi, V. M., Lyne, A. G., Manchester, R. N., Bell, J. F., D'Amico, N., McKay, N. P. F., & Crawford, F. 2000, ApJ, 541, 367
Camilo, F., Ransom, S. M., Halpern, J. P., & Reynolds, J. 2007, ApJ, 666, L93
Camilo, F., Ransom, S. M., Halpern, J. P., Reynolds, J., Helfand, D. J., Zimmerman, N., & Sarkissian, J. 2006, Nature, 442, 892
Carter, J. A., & Read, A. M. 2007, A&A, 464, 1155
Caswell, J. L., McClure-Griffiths, N. M., & Cheung, M. C. M. 2004, MNRAS, 352, 1405
Chevalier, R. A. 2005, ApJ, 619, 839
Chevalier, R. A. 2011, in AIP Conf. Proc., Vol. 1379, Astrophysics of Neutron Stars 2010: A Conference in Honor of M. Ali Alpar, ed. E. Göğüş, T. Belloni, Uuml. Ertan , 5
Crawford, F., Gaensler, B. M., Kaspi, V. M., Manchester, R. N., Camilo, F., Lyne, A. G., & Pivovaroff, M. J. 2001, ApJ, 554, 152
Davies, B., Figer, D. F., Kudritzki, R.-P., Trombley, C., Kouveliotou, C., & Wachter, S. 2009, ApJ, 707, 844
Duncan, R. C., & Thompson, C. 1992, ApJ, 392, L9
Dwarkadas, V. V. 2007, ApJ, 667, 226
Ferrario, L., & Wickramasinghe, D. 2006, MNRAS, 367, 1323
Ferrario, L., & Wickramasinghe, D. 2008, MNRAS, 389, L66
Figer, D. F., Najarro, F., Geballe, T. R., Blum, R. D., & Kudritzki, R. P. 2005, ApJ, 622, L49

Gaensler, B. M., Brazier, K. T. S., Manchester, R. N., Johnston, S., & Green, A. J. 1999, MNRAS, 305, 724
Gaensler, B. M., Manchester, R. N., Staveley-Smith, L., Tzioumis, A. K., Reynolds, J. E., & Kesteven, M. J. 1997, ApJ, 479, 845
Gaensler, B. M., McClure-Griffiths, N. M., Oey, M. S., Haverkorn, M., Dickey, J. M., & Green, A. J. 2005, ApJ, 620, L95
Garcia-Segura, G., Langer, N., & Mac Low, M.-M. 1996, A&A, 316, 133
Gavriil, F. P., Gonzalez, M. E., Gotthelf, E. V., Kaspi, V. M., Livingstone, M. A., & Woods, P. M. 2008, Science, 319, 1802
Geppert, U., Küker, M., & Page, D. 2004, A&A, 426, 267
Geppert, U., Küker, M., & Page, D. 2006, A&A, 457, 937
Gonzalez, M., & Safi-Harb, S. 2003, ApJ, 591, L143
Gonzalez, M., & Safi-Harb, S. 2005, ApJ, 619, 856
Gonzalez, M. E., Kaspi, V. M., Camilo, F., Gaensler, B. M., & Pivovaroff, M. J. 2005, ApJ, 630, 489
Gotthelf, E. V., Vasisht, G., Boylan-Kolchin, M., & Torii, K. 2000, ApJ, 542, L37
Greenstein, G., & Hartke, G. J. 1983, ApJ, 271, 283
Gvaramadze, V. V. 2006, A&A, 454, 239
Heger, A., Fryer, C. L., Woosley, S. E., Langer, N., & Hartmann, D. H. 2003, ApJ, 591, 288
Ho, W. C. G. 2007, MNRAS, 380, 71
Ho, W. C. G. 2012, MNRAS, in press (arXiv:1208.1297)
Ho, W. C. G., Potekhin, A. Y., & Chabrier, G. 2008, ApJS, 178, 102
Kaminker, A. D., Potekhin, A. Y., Yakovlev, D. G., & Chabrier, G. 2009, MNRAS, 395, 2257
Kaspi, V. M. 2010, Proceedings of the National Academy of Science, 107, 7147
Kaspi, V. M., & McLaughlin, M. A. 2005, ApJ, 618, L41
Kumar, H. S., & Safi-Harb, S. 2008, ApJ, 678, L43
Kumar, H. S., Safi-Harb, S., & Gonzalez, M. E. 2012, ApJ, 754, 96
Levin, L., et al. 2010, ApJ, 721, L33
Livingstone, M. A., Kaspi, V. M., & Gavriil, F. P. 2010, ApJ, 710, 1710
Livingstone, M. A., Ng, C.-Y., Kaspi, V. M., Gavriil, F. P., & Gotthelf, E. V. 2011, ApJ, 730, 66
Mereghetti, S. 2008, A&A Rev., 15, 225
Morton, T. D., Slane, P., Borkowski, K. J., Reynolds, S. P., Helfand, D. J., Gaensler, B. M., & Hughes, J. P. 2007, ApJ, 667, 219
Muno, M. P., et al. 2006, ApJ, 636, L41
Ng, C., Slane, P. O., Gaensler, B. M., & Hughes, J. P. 2008a, ApJ, 686, 508
Ng, C.-Y., Gaensler, B. M., Staveley-Smith, L., Manchester, R. N., Kesteven, M. J., Ball, L., & Tzioumis, A. K. 2008b, ApJ, 684, 481
Ng, C.-Y., & Kaspi, V. M. 2011, in AIP Conf. Proc., Vol. 1379, Astrophysics of Neutron Stars 2010: A Conference in Honor of M. Ali Alpar, ed. E. Göğüş, T. Belloni, Uuml. Ertan , 60
Ng, C.-Y., & Romani, R. W. 2008, ApJ, 673, 411
Ng, C.-Y., Romani, R. W., Brisken, W. F., Chatterjee, S., & Kramer, M. 2007, ApJ, 654, 487
Ng, C.-Y., et al. 2011, ApJ, 729, 131
Olausen, S. A., Kaspi, V. M., Lyne, A. G., & Kramer, M. 2010, ApJ, 725, 985
Olausen, S. A., et al. 2012, ApJ, submitted
Page, D., Lattimer, J. M., Prakash, M., & Steiner, A. W. 2004, ApJS, 155, 623
Parent, D., et al. 2011, ApJ, 743, 170
Pavlov, G. G., Shibanov, Y. A., Ventura, J., & Zavlin, V. E. 1994, A&A, 289, 837
Perna, R., & Pons, J. A. 2011, ApJ, 727, L51
Petit, V., Wade, G. A., Drissen, L., Montmerle, T., & Alecian, E. 2008, MNRAS, 387, L23
Pivovaroff, M. J., Kaspi, V. M., Camilo, F., Gaensler, B. M., & Crawford, F. 2001, ApJ, 554, 161
Pons, J. A., Link, B., Miralles, J. A., & Geppert, U. 2007, Physical Review Letters, 98, 071101
Pons, J. A., Miralles, J. A., & Geppert, U. 2009, A&A, 496, 207
Rajagopal, M., Romani, R. W., & Miller, M. C. 1997, ApJ, 479, 347
Rea, N., & Esposito, P. 2011, in High-Energy Emission from Pulsars and their Systems, ed. D. F. Torres & N. Rea (Berlin: Springer), 247
Rea, N., Zane, S., Turolla, R., Lyutikov, M., & Götz, D. 2008, ApJ, 686, 1245
Rea, N., et al. 2009, ApJ, 703, L41
Rea, N., et al. 2010, Science, 330, 944
Reynolds, S. P. 2008, ARA&A, 46, 89
Romani, R. W. 1987, ApJ, 313, 718
Ruderman, M. 1972, ARA&A, 10, 427
Safi-Harb, S., & Kumar, H. S. 2008, ApJ, 684, 532
Scholz, P., Ng, C.-Y., Livingstone, M. A., Kaspi, V. M., Cumming, A., & Archibald, R. 2012, ApJ, in press (arXiv:1204.1034)
Shabaltas, N., & Lai, D. 2012, ApJ, 748, 148
Shibanov, I. A., Zavlin, V. E., Pavlov, G. G., & Ventura, J. 1992, A&A, 266, 313
Thompson, C., & Duncan, R. C. 1993, ApJ, 408, 194
Thompson, C., & Duncan, R. C. 1995, MNRAS, 275, 255
Thompson, C., & Duncan, R. C. 1996, ApJ, 473, 322
Thompson, C., Lyutikov, M., & Kulkarni, S. R. 2002, ApJ, 574, 332
Toalá, J. A., Guerrero, M. A., Chu, Y.-H., Gruendl, R. A., Arthur, S. J., Smith, R. C., & Snowden, S. L. 2012, ApJ, 755, 77
Tsujimoto, M., et al. 2011, A&A, 525, A25
van Adelsberg, M., Heng, K., McCray, R., & Raymond, J. C. 2008, ApJ, 689, 1089
van Adelsberg, M., & Lai, D. 2006, MNRAS, 373, 1495
Vink, J., & Kuiper, L. 2006, MNRAS, 370, L14
Weltevrede, P., Johnston, S., & Espinoza, C. M. 2011, MNRAS, 411, 1917
Weltevrede, P., et al. 2010, PASA, 27, 64
Wilms, J., Allen, A., & McCray, R. 2000, ApJ, 542, 914
Woltjer, L. 1964, ApJ, 140, 1309
Wrigge, M., Chu, Y.-H., Magnier, E. A., & Wendker, H. J. 2005, ApJ, 633, 248
Zavlin, V. E., Pavlov, G. G., & Shibanov, Y. A. 1996, A&A, 315, 141
Zavlin, V. E., Pavlov, G. G., Shibanov, Y. A., & Ventura, J. 1995, A&A, 297, 441
Zhang, L., & Cheng, K. S. 2002, ApJ, 569, 872
Zhang, L., & Jiang, Z. J. 2005, ApJ, 632, 523
Zhu, W., Kaspi, V. M., Gonzalez, M. E., & Lyne, A. G. 2009, ApJ, 704, 1321
Zhu, W. W., Kaspi, V. M., McLaughlin, M. A., Pavlov, G. G., Ng, C.-Y., Manchester, R. N., Gaensler, B. M., & Woods, P. M. 2011, ApJ, 734, 44